nature materials

LETTERS

https://doi.org/10.1038/s41563-019-0600-4

Coexistence of large conventional and planar spin Hall effect with long spin diffusion length in a low-symmetry semimetal at room temperature

Peng Song[1,2,9], Chuang-Han Hsu[1,3,9], Giovanni Vignale[4,5], Meng Zhao[6], Jiawei Liu[1,3], Yujun Deng[7], Wei Fu[1,2], Yanpeng Liu[1,2], Yuanbo Zhang[7], Hsin Lin[8]*, Vitor M. Pereira[1,3]* and Kian Ping Loh[1,2]*

The spin Hall effect (SHE) is usually observed as a bulk effect in high-symmetry crystals with substantial spin–orbit coupling (SOC), where the symmetric spin–orbit field imposes a widely encountered trade-off between spin Hall angle (θ_{SH}) and spin diffusion length (L_{sf}), and spin polarization, spin current and charge current are constrained to be mutually orthogonal. Here, we report a large θ_{SH} of 0.32 accompanied by a long L_{sf} of 2.2 μm at room temperature in a low-symmetry few-layered semimetal $MoTe_2$, thus identifying it as an excellent candidate for simultaneous spin generation, transport and detection. In addition, we report that longitudinal spin current with out-of-plane polarization can be generated by both transverse and vertical charge current, due to the conventional and a newly observed planar SHE, respectively. Our study suggests that manipulation of crystalline symmetries and strong SOC opens access to new charge-spin interconversion configurations and spin–orbit torques for spintronic applications.

With the emergence of quantum materials whose properties are closely related to their underlying symmetry and dimensionality, tuning the interplay between spin–orbit coupling (SOC), crystal symmetry and dimensionality is becoming an interesting route to achieve new properties, such as topological insulating and superconducting ground states in monolayer WTe_2 (ref. [1–4]), nonlinear electrical Hall effect under time-reversal symmetry in few-layered WTe_2 (ref. [5,6]), out-of-plane spin–orbit torque in low-symmetry WTe_2/ferromagnet bilayers[7], out-of-plane spin texture in $SrTiO_3$ two-dimensional (2D) electron gas[8], or a new magnetic spin Hall effect (SHE) arising in the non-collinear antiferromagnet Mn_3Sn[9]. One hitherto unexplored area is how the SHE can be controlled by deliberately defining the interplay between SOC and crystal symmetry. While the SHE allows spin currents to be generated electrically without magnetic fields or ferromagnetic materials, it is usually studied as a bulk effect in high-symmetry crystals, where it encounters two widespread limitations: (1) the trade-off between spin Hall angle (θ_{SH}) and spin diffusion length (L_{sf}) (the latter being small when the former is large), and (2) the stringent requirement of orthogonality between spin polarization, spin current and charge current[10–12].

The key to obtain a large θ_{SH} mostly relies on a strong spin–orbit field, which is usually symmetric in high-symmetry crystals and detrimental of spin coherence, thus yielding short L_{sf} (ref. [10]), irrespective of spin polarization and direction of propagation. For this reason, large θ_{SH} in strong SOC heavy metals, such as Pt, W and Ta[11,13–17] is accompanied with L_{sf} at a length scale of ~10 nm. Meanwhile, the high-mobility semiconductor GaAs has a long L_{sf} up to 8.5 μm, but θ_{SH} is extremely small[18–20]. Thus, there is great interest in finding new band structures that can generate spin currents with high efficiency as well as long spin diffusion lengths. On the other hand, because of the high space group symmetries with at least two mirror symmetries, conventional SHE materials are constrained to have only the spin Hall conductivity (SHC) term σ^z_{xy}, where spin polarization, spin current and charge current are mutually orthogonal. The two limitations have also manifested in a recent observation of SHE in WTe_2 (ref. [21]).

It is well known that the orientation of the spin–orbit field, regarded as an effective magnetic field acting on the spin, is highly constrained by crystalline symmetry[22] and that the allowed forms of intrinsic SHC also depend on the crystal symmetry[22,23]. The essential role of crystal symmetry on the spin–orbit field and allowed intrinsic SHC suggests the possibility to break the two limitations mentioned above through crystal symmetry manipulation. Inspired by the prediction of a large SHE in bulk Weyl semimetals due to their large spin Berry curvature (SBC)[24], we studied the SHE in layered type-II Weyl semimetal candidate T_d-$MoTe_2$ ($MoTe_2$ for brevity)[25,26]. The symmetry breaking in the 2D limit enables the coexistence of a large spin Hall angle ($\theta_{SH} \approx 0.32$) and robust spin diffusion over long distances ($L_{sf} \approx 2.2$ μm) in few-layered $MoTe_2$ at room temperature. These features make $MoTe_2$ one of the most promising candidates for spintronic applications. In addition, an unconventional SHE (designated planar SHE) emerges in low-symmetry few-layered $MoTe_2$, characterized by the coplanar spin polarization, charge current and spin current flow. Using symmetry engineering to break the requirement of orthogonality and induce planar SHE opens a route to accessing unconventional spin–orbit related effects, as well as new device geometries and configurations for spintronic applications.

[1]Centre for Advanced 2D Materials and Graphene Research Centre, National University of Singapore, Singapore, Singapore. [2]Department of Chemistry, National University of Singapore, Singapore, Singapore. [3]Department of Physics, National University of Singapore, Singapore, Singapore. [4]Yale-NUS College, Singapore, Singapore. [5]Department of Physics, University of Missouri, Columbia, MO, USA. [6]Institute of Materials Research and Engineering, Agency for Science, Technology and Research (A*STAR), Innovis, Singapore, Singapore. [7]State Key Laboratory of Surface Physics and Department of Physics, Fudan University, Shanghai, China. [8]Institute of Physics, Academia Sinica, Taipei, Taiwan. [9]These authors contribute equally: Peng Song, Chuang-Han Hsu. *e-mail: nilnish@gmail.com; vpereira@nus.edu.sg; chmlohkp@nus.edu.sg

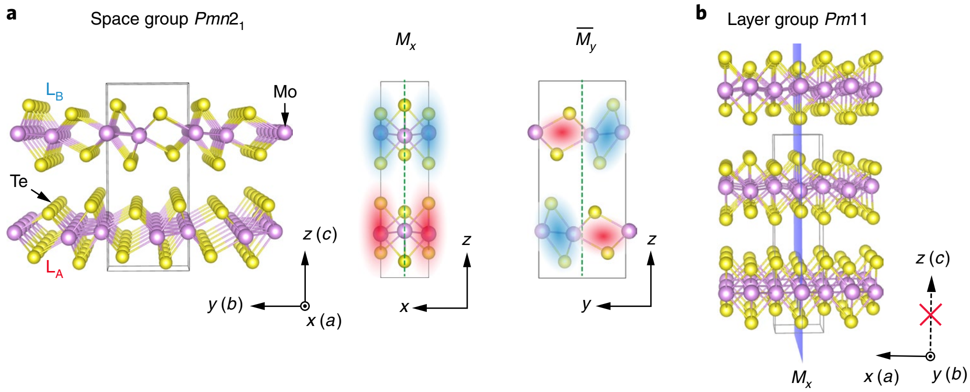

Fig. 1 | Crystal symmetry of bulk and few-layered $MoTe_2$. a, Crystal structure of bulk $MoTe_2$ (L_A and L_B as the bottom and top layer, respectively) and the two mirror symmetries of space group $Pmn2_1$ (no. 31), one is a pure mirror M_x and the other is a glide mirror $\overline{M}_y$ associated with a half translation by $(a+c)/2$. x, y and z are directions along zig-zag, armchair and plane normal of the crystal, with a, b and c being the dimensions of the unit cell in the three directions. **b**, In the 2D system with broken translation symmetry, the crystalline symmetry is described by the layer group $Pm11$ that contains only one mirror plane M_x.

A simple basis for symmetry manipulation is that glide mirror symmetries associated with fractional translations in certain non-symmorphic space groups are broken in 2D realizations. We examine this scenario in $MoTe_2$. The space group of bulk $MoTe_2$ is $Pmn2_1$ (no. 31) with two mirror symmetries (Fig. 1a), a pure mirror M_x, and a glide mirror $\overline{M}_y \equiv \{M_y|\tau\}$ with $\tau = \frac{a+c}{2}$ relating the two monolayers (L_A and L_B) in the unit cell. In the case of few-layered $MoTe_2$, the symmetry is reduced to the layer group ($Pm11$). The original translation symmetry along z is no longer preserved, thus $\overline{M}_y$ is broken (Fig. 1b).

Guided by this reduction of symmetry in few-layered $MoTe_2$, we investigated its SHE using non-local magneto-transport measurements. Rather than performing a direct measurement of non-local signal in a H-bar structure, where substantial non-spin-related behaviour routinely contributes to the non-local signal and causes overestimation of θ_{SH} and L_{sf} (ref. [27–29]), we included a magnetic Co electrode as a passive spin valve to reliably extract the spin-related signal (Fig. 2a). This procedure is inspired by the demonstrated interface spin transfer torque (STT)[30] and its use in a recent observation of the spin Nernst effect[31]. In general, an external magnetic field along z ($B_\perp$) rotates the Co magnetization on demand from its easy axis (y, defined by shape anisotropy) towards z, modulating the interface STT between Co and $MoTe_2$ (as detailed below), thus regulating the amount of spin current that is detected by the non-local contacts. For our subsequent discussion, we note that the introduction of Co does not cause shunting of charge current[32] through $MoTe_2$ because Co electrode does not overlap with charge flow in $MoTe_2$. In all devices, exfoliated few-layered $MoTe_2$ flakes were covered by bilayer h-BN (Supplementary Fig. 1a shows an atomic force microscopy (AFM) image of a bilayer h-BN/5L $MoTe_2$ heterostructure), which serves as a tunnel barrier to suppress direct spin relaxation into Co so that most spin accumulation can be non-locally probed. Due to the much smaller spin resistance (R_S) of ferromagnetic (FM) compared with normal metal ($R_S^{FM}/R_S^{NM} \approx 10^{-2}$)[33,34], direct ohmic contact between Co and $MoTe_2$ would lead to strong spin absorption at the Co–$MoTe_2$ interface[35], which results in substantial suppression of the spin current available for non-local detection. This effect was evidenced by the substantially reduced non-local signal in devices without bilayer h-BN (Supplementary Fig. 4). We note that few-layered $MoTe_2$ exists as orthorhombic T_d phase at room temperature due to a dimensionality-driven phase transition[36], which is also confirmed in our samples by Raman spectroscopy (Supplementary Fig. 1b). All contacts were fabricated along the armchair direction (y) of $MoTe_2$ (polarized Raman spectroscopy in Supplementary Fig. 1c) and show a typical nonlinear current–voltage behaviour (Supplementary Fig. 2) that is consistent with charge tunnelling promoted by the h-BN barrier[37]. Tunnelling charge current through bilayer h-BN is non-zero as long as voltage is applied, suggesting the capability of the spin current to tunnel through the h-BN junction as long as the spin chemical potential is present.

We first explored the conventional SHE, which is governed by the σ_{xy}^z component of the SHC tensor, using the configuration of Fig. 2a with corresponding AFM image in Fig. 2b. Figure 2c shows the $B_\perp$-dependent non-local voltage (V_{NL}) at room temperature. In contrast to the antisymmetric inverse SHE (ISHE) signal induced by ferromagnet-injected spin current[38], we observed V_{NL} to be a symmetric function of $B_\perp$, which is consistent with an intrinsic, SHE-generated spin current with spin polarization independent of the sign of $B_\perp$. V_{NL} gradually increases with the increase of field and saturates when $|B_\perp| > 1.6$ T. The two curves in Fig. 2c show that switching the current direction inverts V_{NL}, a manifestation of intrinsic SHE[10,22], which is further confirmed by the weak temperature dependence of ΔR_{SH} ($\equiv|\Delta V_{SH}/I|$) (Supplementary Fig. 3a) and by the fact that ΔR_{SH} is independent of the amplitude of the injected current (1–50 μA) (Supplementary Fig. 3b)[10]. The slight increase of ΔR_{SH} between 2 and 300 K is attributed to the semimetallic nature of $MoTe_2$ with very small electronic pockets. Therefore, both electron and hole densities are sensitive to thermal broadening of the Fermi–Dirac distribution, which translates into more carriers with rising temperature. This is another feature in line with the intrinsic nature of the observed SHE[10].

The field dependence of V_{NL} in Fig. 2c is understood as follows. $B_\perp$ modulates the ISHE by controlling the interface spin absorption, which results from a STT that depends on the relative orientation of the Co magnetization (**M**) and the spin polarization (**σ**, constant and parallel to z)[30,31,39]. Spin current with **σ** perpendicular to **M** is absorbed by the Co electrode due to STT. When $B_\perp = 0$, **M** is parallel to y and perpendicular to **σ** (upper panel of Fig. 2d), the degradation of the spin current by the STT effect is maximal, leading to minimal spin current detection by non-local Au contacts. Increasing $B_\perp$ gradually rotates **M** from the y to the z direction. As **M** and **σ** become increasingly collinear, the STT-induced spin absorption is gradually reduced, ultimately vanishing when **M** is fully aligned along z for $|B_\perp| > 1.6$ T (consistent with the saturation field of Co derived from anisotropic magnetoresistance in Supplementary Fig. 4). As illustrated in the lower panel of Fig. 2d, this leaves the

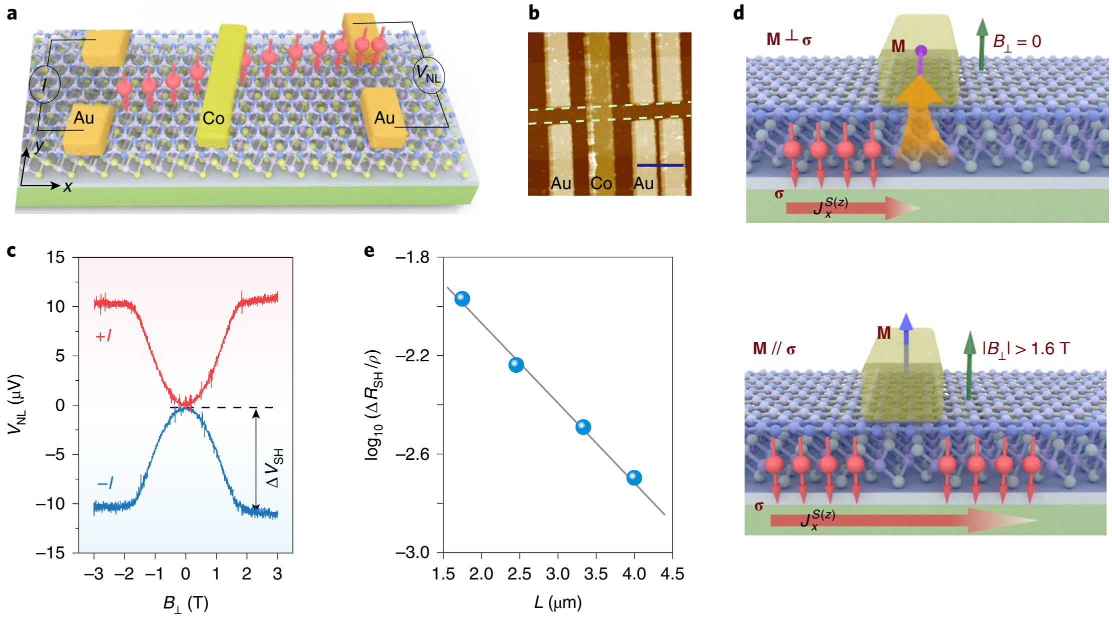

Fig. 2 | Conventional SHE in $MoTe_2$. **a**, Device configuration of bilayer h-BN covered few-layered $MoTe_2$ used to measure SHE. Charge current (I) along y generates $J_x^{S(z)}$ (spin current along x with spin polarization along z, indicated by the red ball with arrow) that diffuses towards the non-local voltage probes, where the ISHE converts it back to a charge current and detected as V_{NL} under open-circuit conditions. The Co nanowire is used to separate the spin-related non-local signal from other contributions. **b**, AFM image of a typical device with dashed lines indicating the channel region. Scale bar is 1 μm. The ratio between channel length and channel width is >3, to ensure negligible ohmic contribution to the non-local signal. **c**, V_{NL} as a function of out-of-plane magnetic field ($B_{\perp}$) for opposite directions of the charge current I, at room temperature. **d**, Schematic illustrations of the interface STT between Co and $MoTe_2$ with $\mathbf{M} \perp \boldsymbol{\sigma}$ (top) and $\mathbf{M} // \boldsymbol{\sigma}$ (bottom), **M** denotes the magnetization of Co and **σ** denotes spin polarization of the spin current diffusing along the x direction ($J_x^{S(z)}$). **e**, Length-dependent ΔR_{SH} ($\equiv|\Delta V_{SH}/I|$) in configuration **a** with a fit to equation (1) (solid line) at room temperature, L is the centre-to-centre distance between current injectors and voltage probes.

maximum spin current to be detected by the non-local contacts when **M** and **σ** are collinear (either parallel or antiparallel). In summary, the absorption of $J_x^{S(z)}$ by the Co electrode is gradually suppressed by increasing $|B_{\perp}|$ and, accordingly, the V_{NL} gradually increases with increasing $|B_{\perp}|$ and saturates when $|B_{\perp}| > 1.6$ T. That the Co electrode acts here as a valve to regulate the amount of spin current that reaches the non-local contacts is further confirmed by the observation that the field dependence vanishes once Co is removed (Supplementary Fig. 6a). To confirm the effect of bilayer h-BN, we performed the same measurement with Co directly deposited on $MoTe_2$, where we observed the same field dependence but the value of ΔR_{SH} decreases to 0.27 Ω (Supplementary Fig. 4). This result supports the fact that most of the spin current is directly relaxed into Co and only a small portion is able to reach the non-local contacts.

Measurements of ΔR_{SH} with non-local contacts placed at different centre-to-centre distances L from the charge injection point were performed to derive θ_{SH} and L_{sf}. ΔR_{SH} measured in such an H-shaped device due to the combined SHE and ISHE is given by[40]

$$\Delta R_{SH} = \frac{1}{2}\theta_{SH}^2 \rho \frac{W}{L_{sf}} e^{-L/L_{sf}} \quad (1)$$

where ρ is the 2D resistivity of the $MoTe_2$ sheet (5.7×10^3 Ω) along the direction of charge flow, and W and L are the width and length of the channel, respectively. Figure 2e shows the length-dependent ΔR_{SH} and a fit to equation (1), which yields $L_{sf} = 1.5$ μm and $\theta_{SH} = 0.32$. The coexistence of long diffusion length and a large spin Hall angle is encouraging and suggests few-layered $MoTe_2$ to be a promising candidate for both spin generation and transport.

In addition to a spin current $J_x^{S(z)}$ induced by charge flowing along y, we show below that charge injection defined by two tunnel contacts parallel to y is also able to generate $J_x^{S(z)}$ with a similar magnitude as that discussed above. This configuration is illustrated in Fig. 3a (AFM image in Fig. 3b), from which the data in Fig. 3 were collected. We first note that the Co electrode here serves the same purpose as in the setup of Fig. 2a, which is a passive spin regulator tuneable by varying $B_{\perp}$ rather than a spin injector, as we demonstrate below. Figure 3c shows V_{NL} versus $B_{\perp}$ at room temperature, where behaviour similar to that in Fig. 2c is observed, and establishing that a spin current $J_x^{S(z)}$ is produced without charge injection along y, that is without contribution from σ_{xy}^z. The out-of-plane spin polarization was confirmed by the angular dependence of ΔR_{SH} (Fig. 3d), which tracks the angular dependence of **M**[31]. Furthermore, we observed spin precession under an in-plane field, which suppresses the out-of-plane component of the diffusing spins and thus reduces the non-local signal generated by the ISHE (Supplementary Fig. 7). Before we discuss in detail the possible origin of this current-induced $J_x^{S(z)}$, we designate it planar SHE to emphasize that, in contrast to the usual SHE scenario, the spin polarization, the direction of flow of the spin current and the charge current all lie in the same plane (xz plane).

We performed length-dependence measurements (Fig. 3e) similar to the ones described above to extract L_{sf} for the planar SHE by fitting to the following equation

$$\Delta R_{SH} = A e^{-L/L_{sf}} \quad (2)$$

where A is a constant. The fitting gives L_{sf} of 2.2 μm at room temperature, proving that the long L_{sf} is robust in $MoTe_2$, irrespective of whether the spin current arises from the conventional or the planar SHE. Figure 3f further demonstrates that ΔR_{SH} only slightly increases with increasing temperature, for the same reason mentioned above.

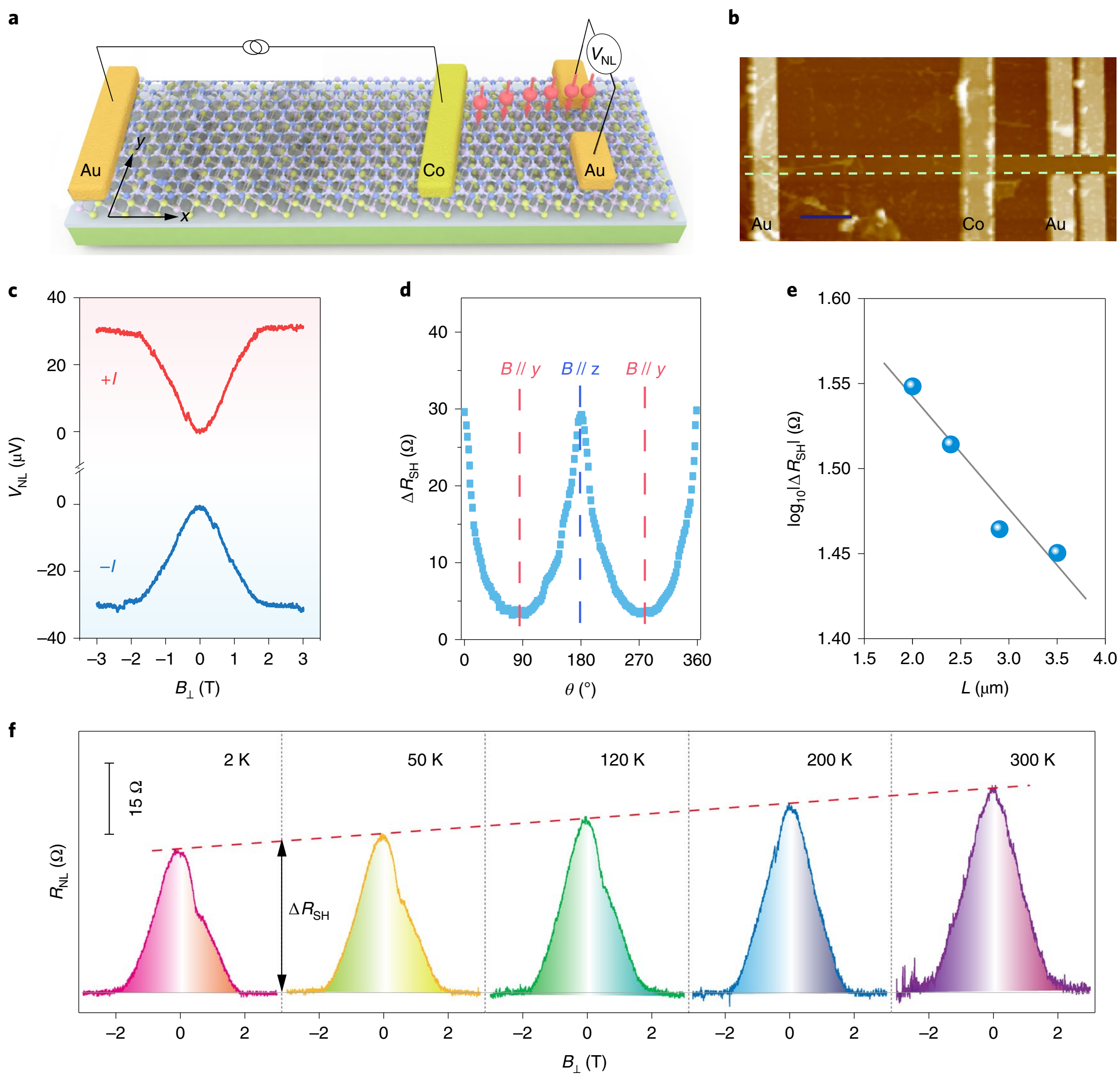

Fig. 3 | Charge-induced out-of-plane spin current. a, Device configuration with non-transverse charge injection. **b**, AFM image of a few-layered $MoTe_2$ device with dashed lines indicating the channel region. Scale bar is 1 μm. **c**, Non-local voltage as a function of out-of-plane magnetic field for opposite current injections at room temperature. Switching the current direction only reverses the sign of the non-local signal. **d**, Angular-dependent ΔR_{SH} when **B** is rotated in the *yz* plane at room temperature. **e**, Semilog plot of length-dependent ΔR_{SH} at room temperature and a fit to equation (2). **f**, Non-local resistance ($R_{NL} \equiv |V_{NL}/I|$) as a function of out-of-plane field at different temperatures. The dashed line is a guide to the eyes to show that there is only weak temperature dependence between 2–300 K.

Other behaviour consistent with an intrinsic SHE, including sign reversal of V_{NL} with current reversal (Fig. 3c) and independence of ΔR_{SH} on the magnitude of the charge current (Supplementary Fig. 8), have been observed as well for the planar SHE. These observations exclude possible contributions by thermal or Nernst effects to ΔR_{SH} and was further validated by second harmonic measurements (Supplementary Fig. 9).

To further confirm that the ΔR_{SH} is dominated by the SHE-induced spin current, and that the Co electrode acts only as a passive spin valve, we performed additional measurements based on the configuration shown in Fig. 4a at room temperature, with disconnected Co electrodes resting between the Au injectors and detectors (AFM image in Fig. 4b). Being clear now that Co can play no role in the generation of the spin current, we observe the same non-local behaviour (Fig. 4d) as in Fig. 3c. Exchanging the current injectors and voltage detectors produced the same result (Fig. 4e), in line with Onsager's reciprocity between SHE and ISHE[10]. The effect of Co as a spin valve was also corroborated by the field independent R_{NL} after removing the Co electrode (Supplementary Fig. 6b). Besides, the similar magnitude of ΔR_{SH} in Figs. 2c and 4d suggests that the θ_{SH} of the conventional and planar SHE should be numerically close, considering that L_{sf} is also close for both SHE components.

Figure 4f compares L_{sf} and θ_{SH} of $MoTe_2$ with those of other typical SHE materials. Heavy metals (Pt, W, Ta)[11,13–17] with strong SOC possess large θ_{SH} but extremely short L_{sf}. On the other hand, high-mobility semiconductors (GaAs, Si)[18–20] show long L_{sf} up to 10 μm, while θ_{SH} is small due to weak SOC. Light metals (Ag, Cu)[16] and recently emerged 2D electron gas (LAO/STO[41,42]) show considerably larger θ_{SH} and long L_{sf} in the submicrometre region. In the case of 2D semimetal $MoTe_2$, large SBC and reduced charge conductivity give rise to θ_{SH} values as large as 0.32. The long L_{sf} extracted from our measurements of $J_x^{S(z)}$ arises from the unique band structure of few-layered $MoTe_2$, in which the spin–orbit field is not only large, but also asymmetric, as evidenced by the recent observation of Ising superconductivity and first-principle calculations[43]. The breaking of the $\overline{M}_y$ symmetry in the few-layered $MoTe_2$ leads to the

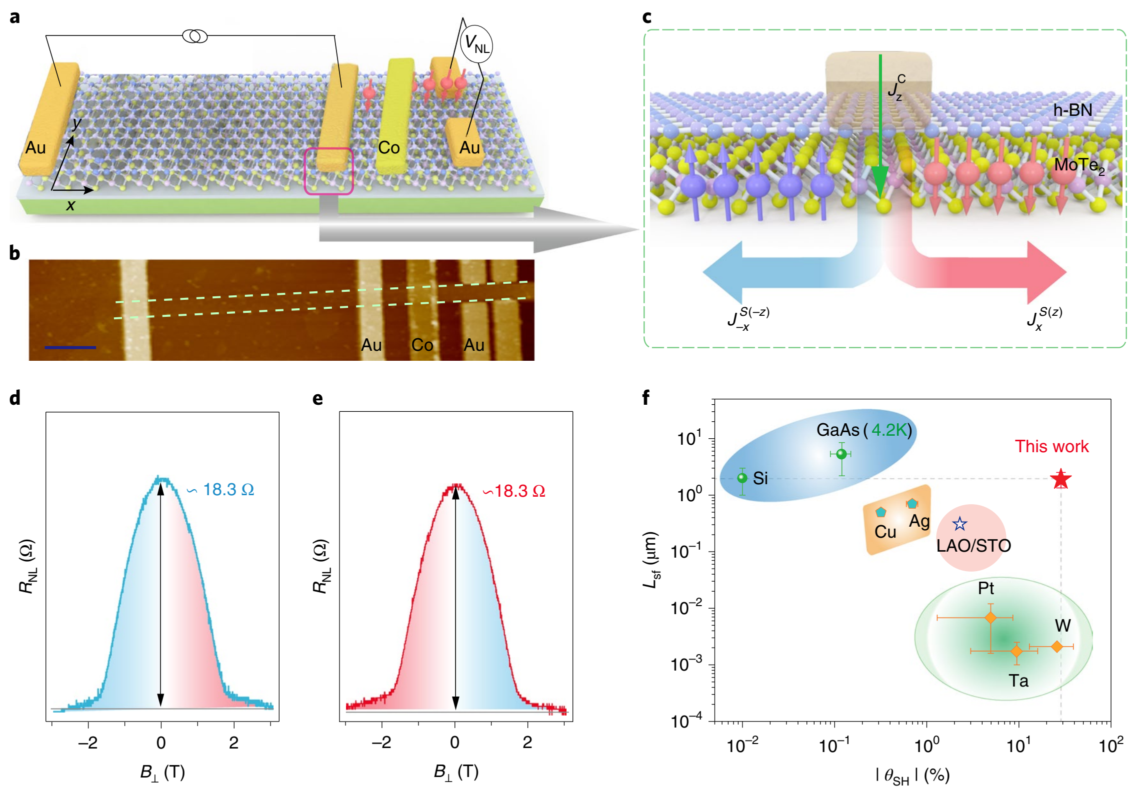

Fig. 4 | Planar SHE and performance benchmark. a, Device configuration where current is injected between two Au contacts. **b**, AFM image of a typical device with dashed lines indicating the channel region. Scale bar is 1 μm. **c**, Schematics of interface charge injection and the planar SHE. **d**, The corresponding R_{NL} as a function of out-of-plane field at room temperature. **e**, Measurement in the same device **a** but swapping the contact pairs used for the charge injection and voltage detection. **f**, Ashby plot of L_{sf} and θ_{SH} of typical SHE materials. Semimetal $MoTe_2$ offers a promising combination of large θ_{SH} and long L_{sf}, compared with most other materials that are normally limited by a trade-off between the two parameters.

large spin–orbit field along z, which results in a dominant out-of-plane spin polarization for the electron pockets[43]. In addition, the large spin splitting at the bottom of conduction band (as calculated in a previous study[44]), and its enhancement in the 2D limit, contributes to further stabilize the spin current against dephasing. Finally, our observation of a long L_{sf} is consistent with previous optical measurements of spin lifetime up to 0.4 ns[44]. More detailed discussion of the possible origin of a long L_{sf} is provided in the Supplementary Information.

To trace the microscopic origin of the charge-induced $J_x^{S(z)}$ in Figs. 3 and 4, we present below a symmetry analysis considering the symmetry breaking in few-layered $MoTe_2$. The results are summarized in Supplementary Table 1, which shows that several unconventional SHC forms can be induced by deliberately breaking crystal symmetries in compounds that would otherwise be limited to the conventional form (that is, σ_{xy}^z). While the two mirror symmetries M_x and $\overline{M}_y$ make the bulk compatible with only the conventional SHC forms (σ_{xy}^z and σ_{yx}^z), the loss of $\overline{M}_y$ allows a number of unconventional SHC forms, in addition to σ_{xy}^z. Among the new symmetry-allowed forms, we believe that σ_{xz}^z is the primary contributor to the $J_x^{S(z)}$. At the interface, we have the injection of charge current along the $-z$ direction (J_z^C), as guaranteed by the fact that this current enters $MoTe_2$ by tunnelling through the h-BN spacer (Fig. 4c). A finite planar spin Hall component σ_{xz}^z generates $J_x^{S(z)} \propto \sigma_{xz}^z J_z^C \neq 0$, which diffuses along $\pm x$ with spin polarization along $\pm z$. As the right-moving ($+x$) spin current travels, the conventional SHC σ_{xy}^z converts it to the transverse voltage (along y) measured between the non-local contacts depicted in the far-right region of Fig. 4a. Note that the spin current that reaches the non-local probes is dominated by the $J_x^{S(z)}$ generated by J_z^C from the injector at the right side, because the distance between the two injectors is usually about 5 μm (see device images in Figs. 3b and 4b), substantially longer than the L_{sf} obtained above. We rule out the contribution from the other non-conventional SHC forms as discussed in the Supplementary Information.

In addition to the symmetry considerations presented above, which are general and can be potentially realized across many materials, we further theoretically quantified both the conventional and the planar SHE in few-layered $MoTe_2$. Supplementary Fig. 10 shows the band structure of a five-layer (5L) slab, on top of which we superimpose the SBC that enters the computation of σ_{xy}^z and σ_{xz}^z. Our calculations show substantial SBC hotspots associated with band crossings in the vicinity of the Fermi level, which are directly related to the large SHC[24]. Figure 5a–d shows the k-resolved SHC in both bulk and a 5L thin film. While σ_{xy}^z is finite and large in both bulk and thin films, σ_{xz}^z is absent in the bulk but acquires a substantial magnitude in the thin films. This proves that the planar SHE is unique to the 2D realizations due to the broken $\overline{M}_y$. Figure 5e,f shows the calculated chemical potential-dependent SHC and θ_{SH}, which are large and comparable for both SHC forms. On the other hand, the charge conductivity of $MoTe_2$ is modest due to the small electron and hole pockets that define its Fermi surface (Supplementary Fig. 10), as well as to the quantum confinement to 2D. This combination of large SHC and small charge conductivity leads to θ_{SH} as high as 0.40 near charge neutrality, which is among the highest known. The magnitudes of SHC and θ_{SH} do not have a strong thickness dependence for the 3–6L slabs we studied (Supplementary Fig. 13), which is particularly important for the planar SHE,

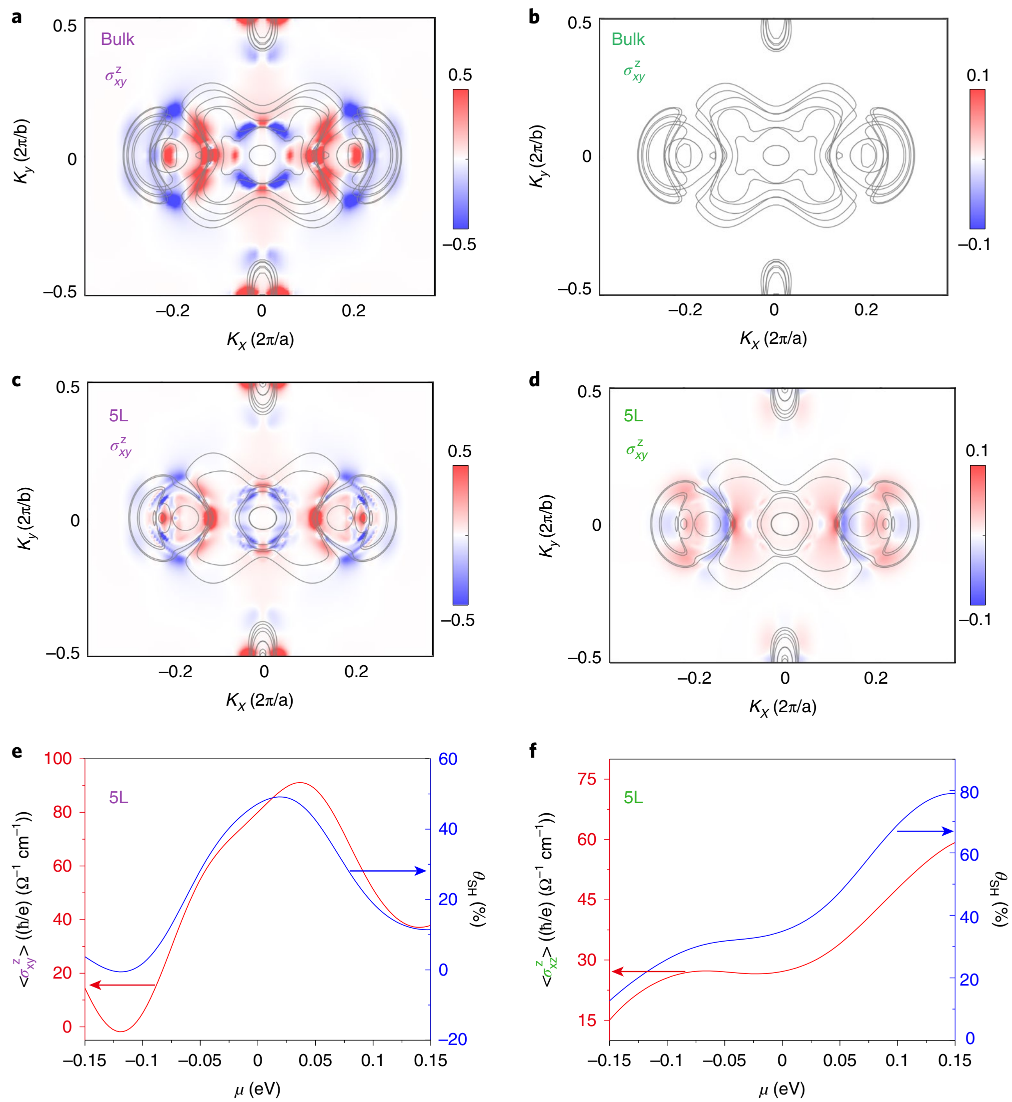

Fig. 5 | DFT calculations of the SHE of MoTe$_2$. a,b, Calculated k-resolved SHC of σ^z_{xy} (**a**) and σ^z_{xz} (**b**) in bulk MoTe$_2$, where the magnitude is integrated with respect to k_z. The grey lines are the Fermi surface contours (at $k_z c/\Pi = 0$, 0.4, 0.6, 1.0 for bulk) and the colour code represents the magnitude of the SHC. **c**,**d**, The same calculation as in σ^z_{xy} (**c**) and σ^z_{xz} (**d**) in 5L MoTe$_2$. **e**,**f**, Calculated SHC of σ^z_{xy} (**e**) and σ^z_{xz} (**f**) for 5L MoTe$_2$ and their corresponding θ_{SH} as a function of chemical potential. All the calculations were done at $T = 300$ K. We obtain $\sigma^z_{xz} \neq 0$ only in the few-layer slabs, in direct agreement with the symmetry constraints that require reducing the symmetry of bulk MoTe$_2$ to generate the planar SHE.

suggesting its robustness is not dependent on a precise number of layers. However, we note the existence of an even-odd effect in σ^z_{xz} (Supplementary Fig. 13b) that arises from an approximate cancellation of the SBC in even-layered slabs (in bulk, neighbouring monolayers have exactly opposite curvature). The close agreement in the magnitude of θ_{SH} derived from experiments and theory confirms that the spin current in Figs. 3 and 4 is primarily generated by the planar σ^z_{xz} and supports the physical picture illustrated in Fig. 2d.

Both our experiments and theoretical analysis demonstrate that lowering the symmetry by simply thinning down semimetal MoTe$_2$ to the few-layer limit is an effective route to access unconventional—yet intrinsic—SHEs, which have not been accessed before, especially in non-magnetic materials. While spin–orbit torques recently observed in a WTe$_2$/ferromagnet bilayer[7] and some antiferromagnets[45–47] also suggest coplanar arrangements of charge current, spin current and spin polarization, their relationship with unconventional SHE has not been clearly established. Previous authors[7] excluded SHE (both conventional and unconventional) as the possible microscopic origin of torques observed in WTe$_2$/ferromagnet bilayers because their symmetry analysis was based on bulk WTe$_2$, instead of the few-layered WTe$_2$ used in their measurements. The spin–orbit torques in antiferromagnets have been ascribed to spin polarization caused by a Dresselhaus-like spin–orbit field in which the antiferromagnetic domains play a main role[48–50], instead of a pure spin current generated by SHE, as we observed here.

In conclusion, we have shown that deliberately lowering the symmetry of the Weyl semimetal candidate MoTe$_2$ leads to a rarely observed coexistence of a large θ_{SH} of 0.32 and a long L_{sf} of 2.2 μm at room temperature. The similarity of Weyl semimetals in terms of their band structure and symmetry reduction in 2D form suggests that they can be promising candidates as both source and conduit of spin current, with the potential to outperform most other spintronic materials. We have also established that engineering the crystalline symmetry is an effective route to achieve new forms of intrinsic SHE, such as the planar SHE reported and quantified here. The realization of planar SHE, and possibly other unconventional forms, greatly enriches the family of SHEs and we anticipate the same principle may be used to expand the range and flexibility of other spin–orbit related effects.

Online content

Any methods, additional references, Nature Research reporting summaries, source data, extended data, supplementary information, acknowledgements, peer review information; details of author contributions and competing interests; and statements of data and code availability are available at https://doi.org/10.1038/s41563-019-0600-4.

Received: 20 June 2019; Accepted: 20 December 2019;
Published online: 03 February 2020

References

1. Wu, S. et al. Observation of the quantum spin Hall effect up to 100 kelvin in a monolayer crystal. *Science* **359**, 76–79 (2018).
2. Fei, Z. et al. Edge conduction in monolayer WTe_2. *Nat. Phys.* **13**, 677 (2017).
3. Fatemi, V. et al. Electrically tunable low-density superconductivity in a monolayer topological insulator. *Science* **362**, 926–929 (2018).
4. Sajadi, E. et al. Gate-induced superconductivity in a monolayer topological insulator. *Science* **362**, 922–925 (2018).
5. Ma, Q. et al. Observation of the nonlinear Hall effect under time-reversal-symmetric conditions. *Nature* **565**, 337–342 (2018).
6. Kang, K., Li, T., Sohn, E., Shan, J. & Mak, K. F. Nonlinear anomalous Hall effect in few-layer WTe_2. *Nat. Mater.* **18**, 324–328 (2019).
7. MacNeill, D. et al. Control of spin–orbit torques through crystal symmetry in WTe_2/ferromagnet bilayers. *Nat. Phys.* **13**, 300 (2016).
8. He, P. et al. Observation of out-of-plane spin texture in a $SrTiO_3$ two-dimensional electron gas. *Phys. Rev. Lett.* **120**, 266802 (2018).
9. Kimata, M. et al. Magnetic and magnetic inverse spin Hall effects in a non-collinear antiferromagnet. *Nature* **565**, 627–630 (2019).
10. Sinova, J., Valenzuela, S. O., Wunderlich, J., Back, C. H. & Jungwirth, T. Spin Hall effects. *Rev. Mod. Phys.* **87**, 1213–1260 (2015).
11. Liu, L. et al. Spin-torque switching with the giant spin Hall effect of tantalum. *Science* **336**, 555–558 (2012).
12. Hirsch, J. E. Spin Hall effect. *Phys. Rev. Lett.* **83**, 1834–1837 (1999).
13. Kimura, T., Otani, Y., Sato, T., Takahashi, S. & Maekawa, S. Room-temperature reversible spin Hall effect. *Phys. Rev. Lett.* **98**, 156601 (2007).
14. Vila, L., Kimura, T. & Otani, Y. Evolution of the spin Hall effect in Pt nanowires: size and temperature effects. *Phys. Rev. Lett.* **99**, 226604 (2007).
15. Pai, C.-F. et al. Spin transfer torque devices utilizing the giant spin Hall effect of tungsten. *Appl. Phys. Lett.* **101**, 122404 (2012).
16. Wang, X., Pauyac, C. O. & Manchon, A. Spin-orbit-coupled transport and spin torque in a ferromagnetic heterostructure. *Phys. Rev. B.* **89**, 054405 (2014).
17. Gómez, J. E. et al. Spin transport parameters in $Ni_{80}Fe_{20}$/Ru and $Ni_{80}Fe_{20}$/Ta bilayers. *Phys. Rev. B.* **90**, 184401 (2014).
18. Garlid, E. S., Hu, Q. O., Chan, M. K., Palmstrøm, C. J. & Crowell, P. A. Electrical measurement of the direct spin Hall effect in Fe/$In_xGa_{1-x}As$ heterostructures. *Phys. Rev. Lett.* **105**, 156602 (2010).
19. Ehlert, M. et al. All-electrical measurements of direct spin Hall effect in GaAs with Esaki diode electrodes. *Phys. Rev. B.* **86**, 205204 (2012).
20. Olejník, K. et al. Detection of electrically modulated inverse spin Hall effect in an Fe/GaAs microdevice. *Phys. Rev. Lett.* **109**, 076601 (2012).
21. Zhao, B. et al. Observation of spin Hall effect in semimetal WTe_2. Preprint at https://arxiv.org/abs/1812.02113 (2019).
22. Sinova, J. et al. Universal intrinsic spin Hall effect. *Phys. Rev. Lett.* **92**, 126603 (2004).
23. Guo, G. Y., Yao, Y. & Niu, Q. Ab initio calculation of the intrinsic spin Hall effect in semiconductors. *Phys. Rev. Lett.* **94**, 226601 (2005).
24. Sun, Y., Zhang, Y., Felser, C. & Yan, B. Strong intrinsic spin Hall effect in the TaAs family of Weyl semimetals. *Phys. Rev. Lett.* **117**, 146403 (2016).
25. Deng, K. et al. Experimental observation of topological Fermi arcs in type-II Weyl semimetal $MoTe_2$. *Nat. Phys.* **12**, 1105–1110 (2016).
26. Jiang, J. et al. Signature of type-II Weyl semimetal phase in $MoTe_2$. *Nat. Commun.* **8**, 13973 (2017).
27. Balakrishnan, J., Kok Wai Koon, G., Jaiswal, M., Castro Neto, A. H. & Özyilmaz, B. Colossal enhancement of spin–orbit coupling in weakly hydrogenated graphene. *Nat. Phys.* **9**, 284–287 (2013).
28. Kaverzin, A. A. & van Wees, B. J. Electron transport nonlocality in monolayer graphene modified with hydrogen silsesquioxane polymerization. *Phys. Rev. B.* **91**, 165412 (2015).
29. Völkl, T. et al. Absence of a giant spin Hall effect in plasma-hydrogenated graphene. *Phys. Rev. B.* **99**, 085401 (2019).
30. Yang, T., Kimura, T. & Otani, Y. Giant spin-accumulation signal and pure spin-current-induced reversible magnetization switching. *Nat. Phys.* **4**, 851 (2008).
31. Meyer, S. et al. Observation of the spin Nernst effect. *Nat. Mater.* **16**, 977–981 (2017).
32. Luqiao Liu, R. A. Buhrman, D. C. Ralph. Review and analysis of measurements of the spin Hall effect in platinum. Preprint at https://arxiv.org/abs/1111.3702 (2012).
33. Valenzuela, S. O. Nonlocal electronic spin detection, spin accumulation and the spin Hall effect. *Inter. J. Mod. Phys. B* **23**, 2413–2438 (2009).
34. Idzuchi, H., Fukuma, Y. & Otani, Y. Spin transport in non-magnetic nano-structures induced by non-local spin injection. *Phys. E.* **68**, 239–263 (2015).
35. Zahnd, G. et al. Spin diffusion length and polarization of ferromagnetic metals measured by the spin-absorption technique in lateral spin valves. *Phys. Rev. B.* **98**, 174414 (2018).
36. He, R. et al. Dimensionality-driven orthorhombic $MoTe_2$ at room temperature. *Phys. Rev. B.* **97**, 041410 (2018).
37. Britnell, L. et al. Electron tunneling through ultrathin boron nitride crystalline barriers. *Nano Lett.* **12**, 1707–1710 (2012).
38. Valenzuela, S. O. & Tinkham, M. Direct electronic measurement of the spin Hall effect. *Nature* **442**, 176–179 (2006).
39. Nakayama, H. et al. Spin Hall magnetoresistance induced by a nonequilibrium proximity effect. *Phys. Rev. Lett.* **110**, 206601 (2013).
40. Abanin, D. A., Shytov, A. V., Levitov, L. S. & Halperin, B. I. Nonlocal charge transport mediated by spin diffusion in the spin Hall effect regime. *Phys. Rev. B.* **79**, 035304 (2009).
41. Lesne, E. et al. Highly efficient and tunable spin-to-charge conversion through Rashba coupling at oxide interfaces. *Nat. Mater.* **15**, 1261–1266 (2016).
42. Ohshima, R. et al. Strong evidence for d-electron spin transport at room temperature at a $LaAlO_3/SrTiO_3$ interface. *Nat. Mater.* **16**, 609–614 (2017).
43. Cui, J. et al. Transport evidence of asymmetric spin–orbit coupling in few-layer superconducting 1Td-$MoTe_2$. *Nat. Commun.* **10**, 2044 (2019).
44. Wang, Q. et al. Room-temperature nanoseconds spin relaxation in WTe_2 and $MoTe_2$ thin films. *Adv. Sci.* **5**, 1700912 (2018).
45. Kurebayashi, H. et al. An antidamping spin–orbit torque originating from the Berry curvature. *Nat. Nanotechnol.* **9**, 211–217 (2014).
46. Ciccarelli, C. et al. Room-temperature spin–orbit torque in NiMnSb. *Nat. Phys.* **12**, 855–860 (2016).
47. Zhang, W. et al. Giant facet-dependent spin-orbit torque and spin Hall conductivity in the triangular antiferromagnet $IrMn_3$. *Sci. Adv.* **2**, e1600759 (2016).
48. Kresse, G. & Hafner, J. Ab initio molecular dynamics for open-shell transition metals. *Phys. Rev. B.* **48**, 13115–13118 (1993).
49. Kresse, G. & Furthmüller, J. Efficiency of ab-initio total energy calculations for metals and semiconductors using a plane-wave basis set. *Comput. Mater. Sci.* **6**, 15–50 (1996).
50. Kresse, G. & Furthmüller, J. Efficient iterative schemes for ab initio total-energy calculations using a plane-wave basis set. *Phys. Rev. B.* **54**, 11169–11186 (1996).

Publisher's note Springer Nature remains neutral with regard to jurisdictional claims in published maps and institutional affiliations.

Methods

Device fabrication and transport measurements. $MoTe_2$ flakes were exfoliated in inert atmosphere from bulk crystals obtained from HQgraphene. Ultrathin exfoliated h-BN flakes were then transferred on $MoTe_2$ flakes in inert atmosphere to avoid degradation. The heterostructure was annealed at 250 °C for 5 h under high-vacuum conditions to form intimate and clean interfaces. AFM was used to determine the thickness of both flakes and the interface of the heterostructures. Raman spectroscopy was used to probe the crystal orientation of $MoTe_2$. E-beam lithography was used to define the electrode pattern. Co (30 nm) was deposited using molecular beam epitaxy under ultrahigh vacuum (~2×10^{-8} mbar) and capped with 6 nm of MgO. Cr/Au (2/80 nm) was deposited using thermal evaporator. Transport studies were performed in an Oxford Teslatron system. Non-local measurements were carried out using a phase-sensitive lock-in amplifier.

Calculation of the intrinsic SHC and spin Hall angle. The linear response that underlies the intrinsic SHE is expressed as

$$J_i^{s(k)} = \sum_j \sigma_{ij}^k E_j$$

which means that a pure spin current $J_i^{s(k)}$ propagating along i with spin polarization along k can be generated by an electric field along j (E_j). The proportionality is established by the SHC tensor, whose Cartesian components are σ_{ij}^k. In Kubo's formalism[22], these can be computed as an integral of the SBC,

$$\sigma_{ij}^\alpha = e\hbar \sum_n \int_{BZ} \frac{dk}{(2\pi)^3} f_{nk} \Omega_{n,ij}^\alpha(k)$$

where the SBC is given by

$$\Omega_{n,ij}^\alpha(k) = -2\,\mathrm{Im} \sum_{n'\neq n} \frac{\langle nk|\ \hat{J}_i^{s(\alpha)}\ |n'k\rangle \langle n'k|\ \hat{v}_j\ |nk\rangle}{(E_{nk}-E_{n'k})^2}$$

Here, $\hat{J}_i^{s(\alpha)}$ and $\hat{v}_j$ are operators for the spin current $j_i^{s(\alpha)} = \frac{\hbar}{4}\{\sigma^\alpha, v_i\}$ and the velocity, respectively, E_n is the band energy of the band indexed by n, and f is the Fermi–Dirac distribution. As described in the main text, the SHC is calculated using a Wannier basis tight-binding model derived from density functional theory (DFT). In a tight-binding Hamiltonian with hopping amplitudes t_{ij}, the current operator[51] is expressed as

$$\hat{J} = -\frac{ie}{\hbar} \sum_{ij} \sum_\sigma (\mathbf{R}_i - \mathbf{R}_j) t_{ij} c_{i\sigma}^\dagger c_{j\sigma}$$

$\mathbf{R}_i$ is the position vector of site i.

Finally, the charge-to-spin conversion efficiency SHE is dictated by the spin Hall angle, which is defined as

$$\theta_{\mathrm{SH}} = \frac{2e}{\hbar}\frac{J^s}{J^c} = \frac{2e}{\hbar}\frac{\sigma_{\mathrm{SH}}}{\sigma_c}$$

where J^s and σ_{SH} represent the magnitudes of the pure spin current and SHC, and J^c and σ_c represent the magnitudes of the charge current and charge conductivity, $\mathbf{J}^c = \sigma_c \mathbf{E}$.

Symmetry-imposed shape of linear response tensors. Consider the linear response with three observables,

$$\sigma_{(\hat{B}_k\hat{C}_i)\hat{A}_j(\omega)} = \int_0^\infty dt\, e^{-i\omega t} \int_0^\beta d\lambda \hat{A}_j \hat{B}_k(t+i\hbar\lambda)\hat{C}_i(t+i\hbar\lambda)$$

where $\hat{A}_j$, $\hat{B}_k$ and $\hat{C}_i$ are three observables, and the response function consists of one combined observable $(\hat{B}_k\hat{C}_i)$ and a single observable $\hat{A}_j$. Following previous studies[52,53], one can obtain the transformation of σ under a unitary symmetry operation $u=\{R|t\}$,

$$\sigma_{(\hat{B}_k\hat{C}_i)\hat{A}_j(\omega)} = \sum_{lmn} \sigma_{(\hat{B}_m\hat{C}_n)\hat{A}_l(\omega)} D_{lj}^{(\hat{A})}(u) D_{mk}^{(\hat{B})}(u) D_{ni}^{(\hat{C})}(u)$$

where R can be any symmetry operation in the point group of the crystal and t is a fractional translation. $D^{\hat{X}}$ is the matrix representation of the symmetry operation $\hat{X}$. In general, the observable operator can be either a polar (spatial) $\hat{P}$ or axial (pseudo) $\hat{A}$ vector. For example, the charge current density is a polar vector and the spin current density is an axial vector. Accordingly, the transformation matrices have different forms,

$$D^{\hat{P}}(u) = D(R), \quad D^{\hat{A}}(u) = \det(R) D(R)$$

The SHE response function σ_{ij}^k corresponds to replacing the charge current J_j^c, spin current $J_i^{s,k}$ for $\hat{A}_j$ and $(\hat{B}_k\hat{C}_i)$, respectively, in the above expressions. To show that the unconventional SHE is forbidden when the system includes two orthogonal mirror symmetries, consider for example the two mirrors M_x and M_y, perpendicular to the x and y directions. The components of the SHC where the spin points along z are related by

$$R = M_x \Rightarrow \sigma_{xy}^z = \sigma_{xy}^z, \quad \sigma_{xz}^z = \sigma_{xz}^z, \quad \sigma_{yz}^z = -\sigma_{yz}^z,$$
$$R = M_y \Rightarrow \sigma_{xy}^z = \sigma_{xy}^z, \quad \sigma_{xz}^z = -\sigma_{xz}^z, \quad \sigma_{yz}^z = \sigma_{yz}^z.$$

this leaves σ_{xy}^z as the only non-zero term allowed by symmetry in the SHC, which is associated with the conventional SHE. In the current study, one of the mirror symmetries is a glide mirror, $\overline{M}_y$ (Fig. 1), which is broken when the translation symmetry along z is lifted in quasi-2D systems. As a result, only the first of the previous set of relations (involving the remaining symmetry M_x) applies, therefore allowing the new, and unconventional, component σ_{xz}^z that we designate planar SHE.

Wannier basis tight-binding Hamiltonian of few-layered T_d-$MoTe_2$. The first-principles tight-binding Hamiltonian of bulk T_d-$MoTe_2$ is built on the basis of the Wannier basis with resort to the VASP ab initio simulation package[48–50] and Wannier90 (ref. [54]). The latter is used to obtain the bulk tight-binding model, which is truncated at the surfaces to describe T_d-$MoTe_2$ flakes with different thickness. Having such a tight-binding formulation allows a straightforward computation of any component of the SHC tensor and θ_{SH} in linear response.

Current-driven non-equilibrium spin accumulation in T_d-$MoTe_2$. In addition to the SHE, spin currents can intrinsically arise from current-induced spin accumulation $\langle\delta S\rangle$ through the inverse spin galvanic effect (ISGE) (refs. [55,56]). In linear response, the spin accumulation averaged over the Fermi surface is given by[57]

$$\langle\delta\mathbf{S}\rangle = \frac{\pi e \tau_{qs}}{V} \sum_n \sum_k \langle nk|\ \sigma\ |nk\rangle \langle nk|\ \mathbf{E}\cdot\nabla_k H_k\ |nk\rangle \delta(\epsilon_f - \epsilon_{nk})$$

where τ_{qs}, ϵ_f and V are the quasiparticle relaxation time, Fermi level and the 2D volume. H_k is the tight-binding Hamiltonian in the Wannier basis, $\langle nk|\ \sigma\ |nk\rangle$ is the spin texture of band n, σ is the vector of Pauli matrices and $\langle nk|\ \mathbf{E}\cdot\nabla_k H_k\ |nk\rangle$ is the group velocity in band n projected onto the external electric field $\mathbf{E}$. The symbol $\langle\delta S_i^\alpha\rangle$ stands for the accumulation of spin pointing along Cartesian direction α under an external field along i. This spin accumulation creates a spin diffusion current, $J_{D,i}^{s(\alpha)} = D\partial_i\langle\delta S_j^\alpha\rangle$, where D is the spin diffusion constant. The efficiency in converting a charge current along j into a current of spins polarized along α that diffuses along i is therefore defined as

$$\theta_{\mathrm{ISGE}} = \frac{J_{D,i}^{s(\alpha)}}{J_j^c}\left(\frac{2e}{\hbar}\right) = \frac{D\ \partial_i\langle\delta S_j^\alpha\rangle}{J_j^c}\left(\frac{2e}{\hbar}\right) = \frac{\langle\delta S_j^\alpha\rangle}{J_i^c}\left(\frac{\lambda_s}{\tau_{sf}}\right)\left(\frac{2e}{\hbar}\right)$$

where $\lambda_s^2 = D\tau_{sf}$ incorporates the spin diffusion length, λ_s, and time, τ_{sf}. In the calculations of θ_{ISGE} shown in Supplementary Fig. 15, we used the experimentally realistic values of momentum relaxation time $\tau_p = 2.74$ fs (obtained from the photoemission experiments[58]) and $\tau_{sf} = 0.4$ ns (from measurements of the relaxation of photoexcited spins ref. [44]).

Finally, calculations of the charge conductivity were performed in the relaxation time approximation, where the longitudinal conductivity (along direction $\hat{\mathbf{x}}_i$) reads

$$J_i^c = \frac{e^2}{h}\frac{2\pi\tau_p E_i}{\hbar V} \sum_n \sum_k \langle nk|\ \partial_{k_i} H_k\ |nk\rangle^2 \delta(\epsilon_f - \epsilon_{nk})$$

where τ_p is the transport relaxation time that we obtain by comparing the experimental and theoretical charge conductivities. Our calculations used the so-obtained values of τ_p along the three crystal axes: $\tau_p^{x(a)} = 1.05$ fs, $\tau_p^{y(b)} = 1.23$ fs and $\tau_p^{z(c)} = 0.96$ fs.

Data availability

The datasets generated by the present study are available from the corresponding author on request.

References

51. Kuzemsky et al. Electronic transport in metallic systems and generalized kinetic equations. *Int. J. Mod. Phys. B.* **25**, 3071–3183 (2011).
52. Kleiner, W. H. Space-time symmetry of transport coefficients. *Phys. Rev.* **142**, 318–326 (1966).

53. Wimmer, S., Seemann, M., Chadova, K., Ködderitzsch, D. & Ebert, H. Spin-orbit-induced longitudinal spin-polarized currents in nonmagnetic solids. *Phys. Rev. B.* **92**, 041101 (2015).
54. Mostofi, A. A. et al. An updated version of wannier90: a tool for obtaining maximally-localised Wannier functions. *Comput. Phys. Commun.* **185**, 2309–2310 (2014).
55. Edelstein, V. M. Spin polarization of conduction electrons induced by electric current in two-dimensional asymmetric electron systems. *Solid State Commun.* **73**, 233–235 (1990).
56. Manchon, A. & Zhang, S. Theory of spin torque due to spin-orbit coupling. *Phys. Rev. B.* **79**, 094422 (2009).
57. Li, H. et al. Intraband and interband spin-orbit torques in noncentrosymmetric ferromagnets. *Phys. Rev. B.* **91**, 134402 (2015).
58. Weber, A. P. et al. Spin-resolved electronic response to the phase transition in $MoTe_2$. *Phys. Rev. Lett.* **121**, 156401 (2018).

Acknowledgements

We acknowledge S. Roche for insightful discussions. K.P.L. acknowledges the AME-IRG grant 'Scalable Growth of Ultrathin Ferroelectric Materials for Memory Technologies', no. A1938c0035, funded by the Agency for Science, Technology and Research, Singapore. P.S. thanks B. Özyilmaz for providing molecular-beam epitaxy slots and H. Chen for assistance in electron-beam lithography.

Author contributions

P.S. and K.P.L. conceived the project, P.S. performed device fabrication and electric measurements with help from Y.D. and Y.Z. C.H.H., H.L., V.M.P. and G.V. performed DFT calculations and theoretical modelling. M.Z. performed Raman measurements and exfoliation of h-BN, J.L. performed MBE deposition of Co, W.F. drew part of the schematics and Y.L. helped with figure processing. P.S., C.H.H., V.M.P. and K.P.L. wrote the manuscript with input from all authors.

Competing interests

The authors declare no competing interests.

Additional information

Supplementary information is available for this paper at https://doi.org/10.1038/s41563-019-0600-4.

Correspondence and requests for materials should be addressed to H.L., V.M.P. or K.P.L.

Reprints and permissions information is available at www.nature.com/reprints.